https://doi.org/10.5194/egusphere-2026-176
Preprint. Discussion started: 9 February 2026

Scale-selective nudging with a diffusion-based filter in the variable-resolution Model for Prediction Across Scales version 8.2.2

Yiyuan Cheng[1,2,3], Jianping Tang[1,2,3]

[1]State Key Laboratory of Severe Weather Meteorological Science and Technology, Nanjing University, Nanjing, 210023, China
[2]Key Laboratory of Mesoscale Severe Weather/Ministry of Education, Nanjing University, Nanjing, 210023, China
[3]School of Atmospheric Sciences, Nanjing University, Nanjing, 210023, China

Correspondence to: Jianping Tang (jptang@nju.edu.cn)

Abstract. Nudged "specified-dynamics" configurations are widely used to align atmospheric models with reanalysis, but their behaviour in unstructured variable-resolution (VR) global models remains poorly understood. Here we implement a diffusion-based spectral nudging scheme in the Model for Prediction Across Scales–Atmosphere (MPAS-A) on a global VR mesh refined over East Asia and evaluate its performance under two convection schemes (Grell–Fritsch and Tiedtke) and a range of filter scales and nudged variables. Full analysis nudging imposes the strongest large-scale constraint and largely erases the scheme-dependent differences, whereas weaker, scale-selective spectral nudging still controls the large scales but allows GF and TK to exhibit distinct behaviours in precipitation frequency and rainband evolution. Kinetic-energy spectra, transient-eddy coherence, and temporal amplitude spectra jointly confirm that the diffusion-based filters act in a clearly scale-selective manner. Overall, our findings suggest that carefully tuned spectral nudging offers an effective trade-off: it keeps the large-scale flow phase-locked to the analysis while preserving enough variability to diagnose how different physics schemes shape the solution.

1 Introduction

Nudging, also known as Newtonian relaxation, is a data assimilation technique that constrains model simulations, ensuring they remain close to a predefined reference state (Anthes, 1974). Initially developed for model initial condition, this approach modifies prognostic equations with additional terms to nudge atmospheric model simulations toward reference fields (Stauffer & Seaman, 1990). Analysis nudging, first introduced by Kao and Yamada (1988), constrains synoptic-scale meteorology in numerical weather models to enable realistic tracer transport and diffusion. Unlike short-range weather forecasts that require frequent reinitialization, nudged simulations can extend beyond predictability time scales. This approach integrates simulations with reanalysis data to guide advection, diffusion, and chemistry models in a physically consistent manner, commonly referred to as a "specified dynamics" configuration (Tweedy et al., 2013; Davis et al., 2022). By aligning model meteorology with observed conditions, nudging facilitates the comparison of model outputs with limited temporal observations under specific meteorological scenarios. Thus, nudging helps mitigate the divergence in sensitivity experiments caused by natural variability, enabling the detection of signals from a significantly smaller dataset compared with free run simulation (Kooperman et al., 2012; Lin et al., 2016; Zhang et al., 2014).

Nudging is frequently used in regional climate models (RCMs) to constrain the degrees of freedom across the entire domain, aligning with the primary assumption that RCMs must reproduce the large-scale background of their driving fields. This approach effectively reduces uncertainties arising from the regional configuration of RCMs and controls internal variability. However, indiscriminate analysis nudging often dampens small-scale variability in RCMs, and excessive nudging can lead to overly convergent results in sensitivity experiments. To address this, spectral nudging techniques have been introduced (Waldron et al., 1996), which restrict RCM freedom at large scales while allowing dynamically consistent small-scale perturbations to evolve within the model. In recent years, numerous sensitivity studies on spectral nudging have been conducted within the context of RCMs. Studies have explored the effects of various factors, including nudging strength,

https://doi.org/10.5194/egusphere-2026-176
Preprint. Discussion started: 9 February 2026

spatial scales, domain sizes, target fields for nudging, and RCM configuration (Alexandru et al., 2009, p. 2009; Miguez-Macho et al., 2004; Schaaf et al., 2017; Separovic et al., 2012; Tang et al., 2017; He et al., 2025).

The design of efficient low-pass filters constitutes a core aspect of spatial scale selection through spectral nudging. In RCMs, real-time spectral decomposition typically necessitates two-dimensional Fast Fourier Transforms (FFTs) to project model operators into spectral space. This process exhibits a strong dependence on quasi-uniform grids with equidistant sampling within the model domain (Miguez-Macho et al., 2004; Storch et al., 2000). Conversely, global spectral models fundamentally represent atmospheric variables (e.g., temperature, wind fields) as linear combinations of spherical harmonics. This framework naturally facilitates spectral nudging implementation at fixed wavenumbers in spectral space, representing one of the earliest numerical approaches for scale selection (Yoshimura & Kanamitsu, 2008). Applying spectral nudging to grid-point global models necessitates specialized filter design. Conventional filters based on physical distance typically require large neighborhoods, potentially demanding access to multiple computational blocks and incurring significant MPI communication overhead. While certain efficient methods exist for specific grid types – for instance, convolution-based spectral nudging applied by Thatcher and McGregor (2009) to separable cubic grids – their general applicability is limited. Their approach decomposed the 2D filter into a product of 1D convolutions along coordinate axes, reducing the computational cost from $O(N^2)$ for direct Gaussian convolution to $O\left(N^{\frac{3}{2}}\right)$, where N denotes the global grid number. Uhe et al. (2015) subsequently extended convolution-based spectral nudging to latitude-longitude grids.

Recent advances in numerical methods have popularized unstructured grids for their ability to accommodate flexible mesh refinement, smooth resolution transitions, and multi-scale features within a unified modelling framework such as Model for Prediction Across Scale-Atmosphere (MPAS-A hereafter, Skamarock et al., 2012). Nudging is originally implemented in MPAS-A by Bullock et al. (2018). But achieving spectral approximation in unstructured grid is still challenging. FFT requires structured data layouts, while efficient convolution filters demand isotropic neighbourhoods, which are incompatible with irregular cell geometries and anisotropic resolutions. Implicit filtering methods (Germano, 1986; Guedot et al., 2015) offer geometric flexibility but incur large computational costs. Solving elliptic equations for implicit filters scales poorly, making real-time applications infeasible for large-scale ocean or climate models (Grooms et al., 2021).

To address these challenges, Grooms et al. (2021) pioneered a diffusion-based filtering framework that iteratively applies discrete Laplacian operators to approximate target kernel behaviours (e.g., Gaussian, boxcar). This method requires only matrix-vector products $O(n_{iter} \cdot N)$ complexity, where n_{iter} is the polynomial order or number of iterations), bypassing expensive linear solves. Critically, it supports arbitrary grid topologies including unstructured meshes by leveraging existing model discretization of scalar/vector Laplacians. The filter's efficiency and adaptability to spatially varying scales enable practical scale-aware analysis beyond the grid resolution, overcoming prior unstructured geometric constraints.

2 Nudging implementation and model configuration

the nudging capability has been ported into MPAS-A version 8.2, based on the earlier implementation originally developed in MPAS-A version 4.0 by Bullock Jr et al. (2018). The nudging technique is designed to gently constrain the model's prognostic variables, denoted as φ_m, toward corresponding values φ_{ref} from an external reference or host dataset, such as reanalysis products (e.g., ERA-Interim).

2.1 Newtonian relaxation

In this study, we employ a nudging framework following Bullock et al. (2018), which is conceptually similar to the scheme described by Stauffer and Seaman (Stauffer & Seaman, 1990) and has been implemented in MPAS-A.

$$\frac{\partial \varphi_m}{\partial t} = \mathbb{F}(\varphi_m) + G_\alpha W(z, reso) \cdot (\varphi_{ref} - \varphi_m), \quad (1)$$

https://doi.org/10.5194/egusphere-2026-176
Preprint. Discussion started: 9 February 2026

The above equation represents the prognostic equation for the variable φ with an added nudging tendency term. Here, $\mathbb{F}$ denotes the native model tendency, and G_α is the nudging inverse timescale (or "nudging coefficient"), which in the design of Bullock et al. (2018) is chosen to match the characteristic error growth timescale at the mesoscale α. W is a dimensionless weighting profile that depends on the vertical level z and the model resolution $reso$, and is used to modulate the strength of nudging in the vertical and across scales.

The relaxation tendency is treated as a physical process within the MPAS-A physics suite and is applied after all other parameterization tendencies have been computed. Because MPAS-A uses an unstructured polygonal computational mesh, some preprocessing is required to map the reference fields onto the model grid. This is achieved by augmenting the standard MPAS-A initialization/preprocessing to produce the necessary scalar variables at cell centers based on the reanalysis data. At each model time step, the model checks whether it is time to update the target fields. When an update is due, a new target field derived from ERA-Interim at a 6-hour interval is introduced, and the target fields are then linearly interpolated in time between consecutive analysis times.

$$\varphi_m{}^{n+1} = \varphi_m{}^{n} + \Delta t \cdot G_\alpha W(z, reso) \cdot \left((1-\delta) \cdot \varphi_{ref}^{old} + \delta \cdot \varphi_{ref}^{new} - \varphi_m{}^{n} \right), \quad (2)$$

Here, δ is defined from the relative position of the model time within two consecutive target fields, i.e. $\delta = \frac{(t^n - t_{old})}{t_{ref}}$. This linear update of the reference field effectively prevents the artificial accumulation of nudging increments on the 6-hour timescale and yields a smoother evolution of the spatial correlations than a step-function approach, in which the target field is only updated at the analysis times (Sun et al., 2019).

2.2 Spatial filter for spectral nudging

Traditional spatial filtering typically employs convolution kernels of the form:

$$f_{filtered(x)} = \int_\Omega G(x - x') f(x') dx', \quad (3)$$

where G is a convolution kernel (e.g., Gaussian) acting as a low-pass filter, $f_{filtered(x)}$ is the filtered signal or field at location x, and $f(x')$ is the original signal at location x'. The diffusion-based filter developed by Grooms et al. (2021) extends this concept to geometries or grids where Fourier modes are not readily available by leveraging the spectral properties of a discrete Laplacian operator L. Specifically, using the eigen-decomposition:

$$L\, q_i = -k_i{}^2 q_i \quad (4)$$

Where$\{q_i\}$are the eigenvectors and$\{k_i^2\}$the corresponding eigenvalues, the Laplacian operator Δ acts as a frequency-sensitive differential operator in the context of Fourier analysis.

Filtering can then be defined in the eigenbasis q_i as:

$$f_{filtered} = p(-L)f = \sum_{i=1}^{N} p(k_i{}^2) \hat{f}_i q_i \quad (5)$$

Where f is the original discrete signal or field defined on the spatial mesh, $p(-L)$ is a polynomial filter operator constructed from the discrete Laplacian L, $\hat{f}_i = q_i^\top f$ is the projection coefficient of f onto the i-th eigenvector q_i (i.e., the spectral component), $p(k_i^2)$is the filter weight applied to spectral mode i based on eigenvalue k_i^2, N is the total number of spectral modes (equal to the grid size), and q_i is the i-th eigenvector of L, representing a spectral basis function.

This approach constructs a spatial filter by applying a polynomial function of the discrete Laplacian operator, $p(-L)$. By interpreting the eigenmodes of L as generalized analogs of Fourier modes, the method enables spectrally selective filtering even on complex, non-Euclidean domains. The filter shape is encoded in the polynomial p, which approximates a target spectral response and can be efficiently applied through repeated sparse matrix operations. The polynomial p is formulated as a constrained optimization problem solved Galerkin method, which provides a spectrally accurate framework with essential boundary conditions. Grooms et al. (2021) provided a detailed explanation in the appendix on how to obtain the

https://doi.org/10.5194/egusphere-2026-176
Preprint. Discussion started: 9 February 2026

coefficients of a polynomial.Building on the GCM-filter Python implementation (Loose et al., 2022), we developed polynomial coefficients for Taper and Gaussian filter shapes for MPAS-A by applying the diffusion operator. These coefficients can be computed during the simulation by specifying the number of polynomial iterations n_{iter} in the namelist. For the Gaussian filter, the filter scale corresponds to the standard deviation of the Gaussian kernel. The Taper filter is more complex in definition but shares the same interpretation of filter scale: it corresponds to the width of a qualitatively similar boxcar filter. Moreover, with increased polynomial iteration steps, the Taper filter achieves greater scale selectivity than the Gaussian filter, better preserving scales larger than the filter scale while more effectively removing smaller scales.

To account for resolution-dependent anisotropy for the variable resolution mesh, the diffusion operator is designed in the form: $\Delta \rightarrow \nabla \cdot (\kappa(x)\nabla f)$, $\kappa(x)$ is the local anisotropic diffusivity. For the reasons detailed in Grooms et al. (2021), the local filter scale $\kappa(x)$ must satisfy the condition: $\kappa(x)$ and at least one place in the domain where $\kappa(x) = 1$. To ensure scale consistency across the variable-resolution mesh, the anisotropic scaling factor is normalized relative to the maximum horizontal cell area:$\kappa(x) = \frac{A(x)}{A_{\max}}$. In simulations with variable-resolution meshes, the filter scale is defined based on the coarsest grid spacing, and anisotropic diffusion is applied using a spatially varying diffusivity coefficient κ.

In the practical implementation of spatial filtering within MPAS-A, an important consideration is the communication overhead associated with traditional convolution operations. Since global information is not retained on individual processors, the Message Passing Interface (MPI) is employed to gather the distributed arrays from each processor into a global array and redistribute them. The communication cost of this operation scales proportionally with the number of grid points covered by the convolution kernel, approximately $O(N^2)$, where N is the global grid number. When the domain is highly partitioned across many MPI ranks, the convolution stencil may span multiple processor boundaries, requiring complex data gathering and stitching across several blocks. This introduces substantial MPI overhead in traditional convolution-based filtering on unstructured meshes. By contrast, the diffusion-based filtering algorithm reformulates the filtering operation as a sequence of n_{iter} local diffusion steps, effectively approximating the global convolution via a polynomial operator applied to the discrete Laplacian. In MPAS-A, diffusion of scalar variables defined at cell centers utilizes only local information—specifically, values from neighboring cells—allowing a second-order accurate discrete Laplacian to be constructed (Skamarock et al., 2012). Each diffusion step therefore requires only halo exchanges between neighboring blocks, avoiding expensive global communication. The total communication cost for the diffusion-based approach scales as $O(n_{iter}N)$, which is significantly lower than traditional convolution for sufficiently small n_{iter} Empirical tests at 25 km resolution indicate that achieving sub-1% accuracy for a 1000 km-scale Taper filter requires fewer than $n_{iter} \sim 1e^2$ iterations. The model integration without halo design will lead to the growth of small-scale obvious wind speed anomalies in the spectrum. Thus, for practical error tolerances, diffusion-based filtering provides a highly efficient mechanism for extracting large-scale features in MPI-parallel simulations on unstructured meshes. In our implementation, the filter is applied in situ at each model time step, enabling real-time extraction of large-scale state fields from MPAS-A simulations. To ensure consistency and correctness across threads, OpenMP barriers are used to synchronize all threads before and after the halo exchange. This strategy guarantees that each diffusion step completes globally before the next iteration begins, enabling stable and scalable filtering across parallel blocks.

2.3 Experiment design

All experiments are performed with MPAS-A version 8.2, a fully compressible, nonhydrostatic atmospheric model formulated on an unstructured spherical centroidal Voronoi tessellation (SCVT) mesh. We employ a 92–25 km variable-resolution grid together with an anisotropic diffusion-based filter nudging technique applied on this unstructured mesh. The refined region is centered at (105°E, 33.5°N), and the finest ≈25 km resolution covers most of East Asia. MPAS-A uses a terrain-following geometric-height vertical coordinate (Klemp, 2011) with 55 vertical levels and a model top at 30 km. A

https://doi.org/10.5194/egusphere-2026-176
Preprint. Discussion started: 9 February 2026

continuous year-long integration for 2012 is carried out and used to evaluate and compare the different nudging configurations.

To examine how nudging constrains the flow under different physics configurations, and how it interacts with the intrinsic model variability, we consider two standard MPAS-A physics suites that differ mainly in their convective parameterizations: one using the Tiedtke scheme (hereafter TK) and the other using the Grell–Fritsch scheme (hereafter GF). These two configurations are selected to sample distinct representations of moist convection, allowing us to assess the sensitivity of the nudging behavior to the underlying physics package. The main distinction lies in convection treatment across different resolutions. Tiedtke prioritizes removing instability at the parameterized level, while Grell–Freitas retains its scale-awareness, potentially altering the partitioning between parameterized and large-scale precipitation. Table 1 illustrates the detailed configurations.

Table 1 main parameterization schemes of MPAS-A

Parameterization	TK Scheme	GF Scheme
Convection	New Tiedtke (Zhang et al. 2011)	Grell-Freitas (Grell & Freitas, 2014)
Microphysics	WSM6 (Hong and Lim 2006, p. 6)	non-aerosol aware Thompson (Thompson et al., 2008)
Land surface	Noah (Chen and Dudhia 2001)	Noah (Chen and Dudhia 2001)
Boundary layer	YSU (Hong et al. 2006; Hong 2010)	MYNN (WRF 3.6.1)
Surface layer	Monin-Obukhov (WRF 4.0.3)	MYNN (WRF 3.6.1)
Radiation, LW	RRTMG (Iacono et al., 2000; Mlawer et al., 1997)	RRTMG (Iacono et al., 2000; Mlawer et al., 1997)
Radiation, SW	RRTMG (Iacono et al. 2008)	RRTMG (Iacono et al. 2008)

Table 1. Detailed configurations for two physical suites

To conduct a nudging simulation, the user needs to make the following configurations:

All experiments use the European Centre for Medium-Range Weather Forecasts (ECMWF) ERA-Interim reanalysis (Dee et al., 2011) both as initial conditions and as the source of the nudging target fields. ERA-Interim has a horizontal resolution of 0.75°, and all simulations are initialized from ERA-Interim and relaxed toward it every 6 h. The target field is updated by reading the analysis valid 6 h ahead; within the intervening 6-h window, the target fields are linearly interpolated in time, ensuring a smooth temporal evolution of the reference state for nudging. The model results are also evaluated against ERA-Interim at the end of the integrations.

The nudging strength is controlled by the coefficient G_α. In this study, we adopt the default nudging coefficient implemented in MPAS-A, namely $3.0 \times 10^{-4}\ s^{-1}$ for all variables, consistent with the WRF configuration. The choice of this value follows the theoretical argument of Stauffer and Seaman (1990), who relate the nudging timescale to the characteristic timescale of meso-α scale meteorological disturbances. The vertical weighting function W is set to zero below the fifth model level and within the planetary boundary layer (PBL), so that the lowest tropospheric levels remain relatively unconstrained and can develop sufficient internal variability.

The nudging tendency is implemented in MPAS-A as an additional physics tendency, computed on each cell at every time step. The configuration in which this tendency is applied with uniform strength across the entire domain is referred to as analysis nudging in the following. We apply a scale-selective filter directly to the nudging tendency at every time step. Different filter shapes (taper and gaussian) are used to modulate the spectral response of the nudging, and the corresponding experiments are labelled accordingly.

The choice of nudged variables is as follows. Nudging is applied to potential temperature (Θ), water vapor mixing ratio (q_v), and the horizontal wind field. Scalar variables such as Θ and q_v are naturally defined at cell centers and can therefore be nudged directly. In contrast, special care is required for the wind field because, in MPAS-A, the prognostic wind variable is

https://doi.org/10.5194/egusphere-2026-176
Preprint. Discussion started: 9 February 2026

stored as the normal component at cell edges rather than as zonal and meridional components at cell centers. We use the reconstructed zonal and meridional wind components at cell centers (UReconstructZonal and UReconstructMeridional) as the basis for computing the nudging tendencies. Working at cell centers also facilitates consistent application of Laplacian operators to both wind and scalar variables.

The filter strength is controlled through a diffusion-based filtering operator applied to the nudging tendency fields. For each experiment, the number of diffusion iterations is prescribed in the namelist to ensure sufficient convergence of the filter. The shape of the filter is specified by selecting different polynomial forms, which determine the corresponding coefficients in spectral space. Only the nudging tendencies are filtered at each time step; the filtered tendencies are then added to the model's dynamical tendencies. After each application of the diffusion operator, a global halo exchange is performed, and MPI is used to guarantee that all subdomains complete the same number of iterations and halo updates before proceeding to the next iteration. Although the filter is computationally efficient and would in principle allow for many iterations, we estimate the filtering error a priori and select the iteration counts accordingly. In this way, we keep the deviation from the target filter response within approximately 1% across all configurations, ensuring a fair comparison among different filter settings.

We focus our analysis on Gaussian and taper filters with nominal cutoff scales of 500, 1000, and 2000 km. Additional GF experiments using a 3400 km taper filter and 1000km taper configurations with simultaneous nudging of wind and moisture (uvq) or wind and temperature (uvt) are only employed to illustrate basic-state biases. The experimental configurations are summarized in Table 2.

case name	physics scheme suite	filter method	filter scale in km	nudged_variables	nsteps
freerun_GF	GF	freerun		/	/
analysis-uv_GF	GF	analysis		uv	/
taper500km-uv_GF	GF	taper	500	uv	30
taper1000km-uv_GF	GF	taper	1000	uv	43
taper1000km-uvt_GF	GF	taper	1000	uvt	43
taper1000km-uvq_GF	GF	taper	1000	uvq	43
taper2000km-uv_GF	GF	taper	2000	uv	85
taper3400km-uv_GF	GF	taper	3400	uv	147
gaussian500km-uv_GF	GF	gaussian	500	uv	20
gaussian1000km-uv_GF	GF	gaussian	1000	uv	20
gaussian2000km-uv_GF	GF	gaussian	2000	uv	30
freerun_TK	TK	freerun		/	/
analysis-uv_TK	TK	analysis		uv	/
taper500km-uv_TK	TK	taper	500	uv	30
taper1000km-uv_TK	TK	taper	1000	uv	43
taper2000km-uv_TK	TK	taper	2000	uv	85
gaussian500km-uv_TK	TK	gaussian	500	uv	20
gaussian1000km-uv_TK	TK	gaussian	1000	uv	30
gaussian2000km-uv_TK	TK	gaussian	2000	uv	30

Table 2. List of cases and key nudging setups in this study.

3 Data

We use the following observational and reanalysis datasets to drive and validate the model:

(1) The European Centre for Medium-Range Weather Forecasts (ECMWF) ERA-Interim reanalysis (Dee et al., 2011) with a horizontal resolution of 0.75° is used to evaluate the large-scale circulation, including winds, moisture, geopotential height, and CAPE. The near-surface air temperature from ERA-Interim is also incorporated to complement the observational

https://doi.org/10.5194/egusphere-2026-176
Preprint. Discussion started: 9 February 2026

temperature datasets. In addition, ERA-Interim provides the initial conditions for all simulations, supplies the 6-hourly target fields for atmospheric nudging, and is used to update the sea surface temperature every 24 hours. Throughout this study, ERA-Interim serves as the primary reference for assessing the simulated large-scale atmospheric circulation.

(2) The GPCP Daily Version 1.3 Combined Precipitation Dataset (hereafter GPCP1DD), released on 15 September 2017, provides daily precipitation estimates from October 1996 to the present on a 1.0° latitude–longitude grid. It combines satellite-based retrievals with in situ gauge observations, yielding a globally consistent and quality-controlled product for assessing precipitation characteristics. In this study, GPCP1DD is used as the primary reference for evaluating the spatial distribution of precipitation and the daily precipitation frequency simulated by the model.

(3) The Integrated Multi-satellitE Retrievals for GPM (IMERG), a Level-3 product of the Global Precipitation Measurement (GPM) mission, is a merged satellite precipitation dataset that integrates observations from multiple satellite platforms (Huffman et al., 2014). It provides precipitation estimates at 30-minute intervals on a 0.1° × 0.1° grid. In this study, we use the IMERG V06B Final Run product (IMERG-F), which is the post–real-time, fully gauge-adjusted version and is generally considered the most suitable IMERG product for evaluation. IMERG-F is employed to assess the sub-daily and high-resolution characteristics of precipitation, including its spatial patterns and intensity–frequency distributions over the refined domain.

(4) The NOAA Climate Data Record (CDR) of daily mean outgoing longwave radiation (OLR) provides global 1° × 1° gridded fields from 1 January 1979 onward, with a two-day latency. OLR is retrieved directly from radiance observations under all-sky conditions, and additional measurements from imagers aboard international geostationary satellites are incorporated to improve sampling of the diurnal cycle. We use version 1.2 of the Daily OLR CDR to evaluate the large-scale convective activity and cloud–radiative signatures associated with the simulated precipitation and circulation.

4 Results

4.1 Deviations in the Environmental Background

The first step is to examine the variables that are directly constrained by the nudging procedure. Figure 1 shows the 200-hPa zonal-wind errors relative to ERA-Interim, averaged over the year 2012. In the freerun cases, both hemispheres exhibit a pronounced mid-latitude positive bias, with zonal-wind speeds overestimated by more than 6 m s^{-1}, indicates that the model tends to simulate an overly strong upper-level jet The TK physics suite reduces this bias, yet introduces substantial negative biases exceeding –10 m s^{-1} in the subtropics. These negative anomalies are particularly prominent over the refined-mesh East Asia region. By nudging the free model solution toward ERA-Interim, the mid-latitude jet intensity error is reduced to within about 1 m s^{-1}, and the residual error patterns become very similar between GF and TK. Once the large-scale dynamical state is strongly constrained, the role of parameterization-induced circulation drift is strongly diminished. For the cases applying spatial filtering at 500, 1000, and 2000 km, the smoothing nudging term preserves banded structures of positive wind-speed bias of up to 4 m s^{-1}.

https://doi.org/10.5194/egusphere-2026-176
Preprint. Discussion started: 9 February 2026

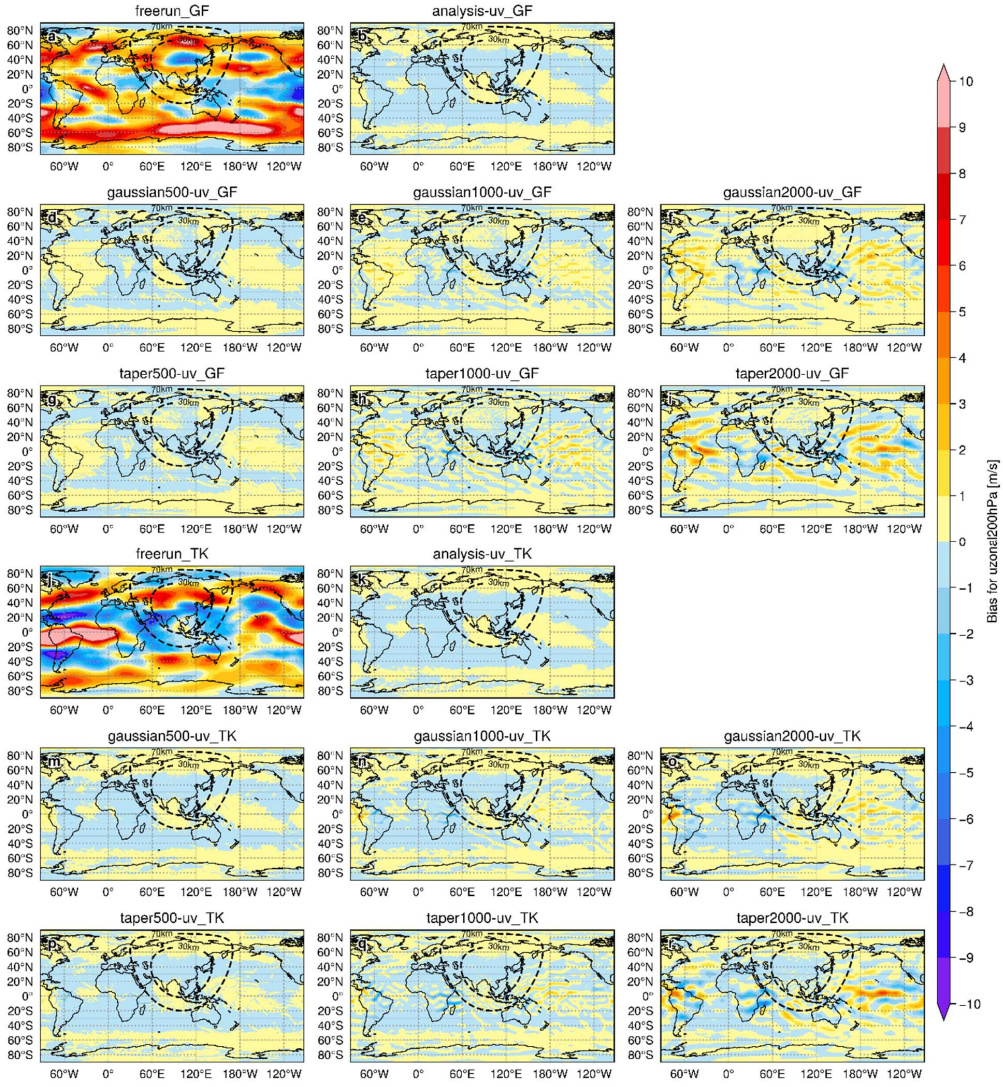

Figure 1. Global patterns of the 2012 annual-mean 200 hPa zonal wind bias relative to ERA-Interim with the GF physics suite in the first three rows and the TK physics suite in the last three rows.

Figure 2 summarize the normalized RMSE (nRMSE) for multiple variable including wind speed, vorticity, top of atmosphere outgoing outgoing longwave radiation (OLR, hereafter), precipitable water, MSLP, and precipitation separately evaluated over the refined (≤80 km) and coarse (>80 km) resolution regions. Values that improve relative to the analysis nudging cases are highlighted with black frames suggesting potential benefits from the model's freedom degree. The corresponding nRMSE fields are normalized by the observed standard deviation to provide a consistent metric across variables. For wind speed, in particular, the analysis nudging cases exhibits the strongest control, representing an approximate upper bound on the achievable correction. The taper3400-uv_GF shows almost no improvement relative to the freerun_GF, indicating that nudging is effectively disabled at this scale. Overall, the spectral nudging cases with filter lengths below 2000 km show that the upper-tropospheric wind field is very effectively constrained. In contrast, the lower-tropospheric winds exhibit substantially larger inter-experiment variability, with nRMSE values roughly doubling from the 500 km to the 2000 km filter cases. The wind field also demonstrates a highly systematic response to increasing nudging strength. When comparing the refined and coarse grid regions, the most pronounced contrast arises in the 500-hPa vorticity

https://doi.org/10.5194/egusphere-2026-176
Preprint. Discussion started: 9 February 2026

(vort500). Even under analysis nudging, the improvement in vort500 remains limited, indicating that this field is dominated by internal mesoscale dynamics that are not strongly corrected by nudging. Introducing additional nudged variables has a robust beneficial effect on the wind field. However, introducing potential temperature (Taper1000-uvt_GF) produces the worst precipitation nRMSE among all cases. Theta nudging disrupts the internal thermodynamic–convective balance in GF. In contrast, adding moisture nudging (Taper1000-uvq_GF) yields the best performance among the GF spectral nudging cases with notably improved nRMSE for precipitation, OLR, precipitable water, and MSLP.

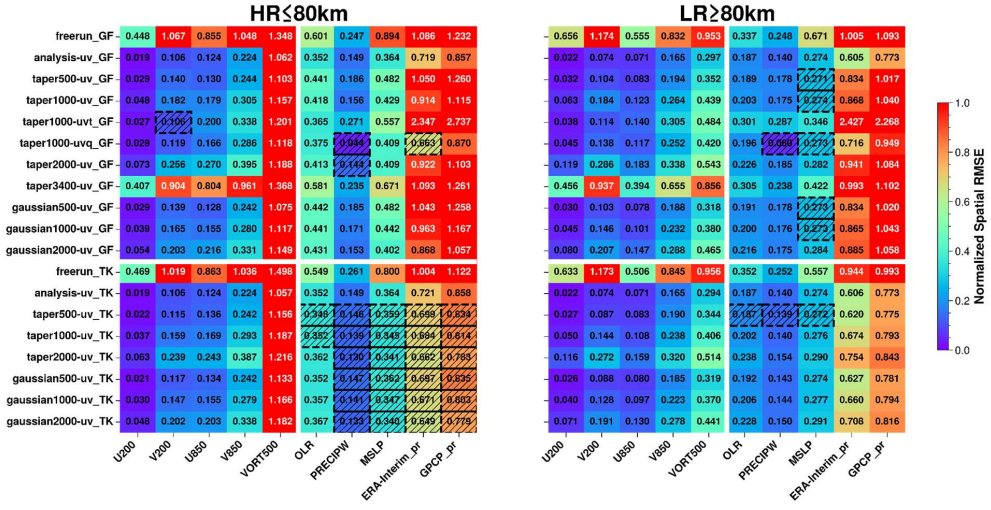

Figure 2. Normalized RMSE (nRMSE) over the refined region (≤80 km, left panels) and the coarse region (>80 km, right panels). The variables include 200 hPa and 850 hPa wind speed (U200, V200, U850, V850), 500 hPa relative vorticity (VORT500), and single-level fields: outgoing longwave radiation (OLR), column-integrated precipitable water (PRECIPW), mean sea level pressure (MSLP), precipitation relative to ERA-Interim (ERA-Interim_pr), and precipitation relative to GPCP (GPCP_pr).

4.2 Spatial–Temporal Patterns of Precipitation Distribution

Precipitation acts as a key conduit through which large-scale circulation adjustments feed back onto the model's moist processes, the nudging cases provide a direct framework for diagnosing this feedback. Figure 3 presents longitude–time cross-sections of daily precipitation, averaged zonally over the deep tropics (10° N–10° S) and between 60° E and 90° W. Each panel shows the precipitation patterns from a specific case, together with its Bias, RMSE, and spatial correlation relative to the reference. In the freerun cases, the two physics schemes display distinct baseline behaviors. The GF scheme exhibits generally smaller mean biases, but its RMSE is consistently above 4.1 mm day^{-1} reflecting substantial errors in the variability and propagation of the convective signal. The TK suites, though marked by a drier mean bias, tends to produce lower RMSE and slightly more coherent temporal structures. The analysis nudging cases impose strong constraints on circulation. Under such conditions, nearly all scheme-dependent differences vanish. GF and TK converge to nearly identical patterns and statistical scores. The cross-sections display closely aligned convective envelopes and propagation features. Under stronger nudging cases (e.g., Taper500-uv_GF and Gaussian500-uv_GF), the GF suites tend to amplify its wet bias, degrading the RMSE despite the tighter dynamical constraint. TK responds more favourably. Stronger nudging drives it closer to the analysis-uv_TK baseline, yielding reduced errors and improved pattern correlations.

https://doi.org/10.5194/egusphere-2026-176
Preprint. Discussion started: 9 February 2026

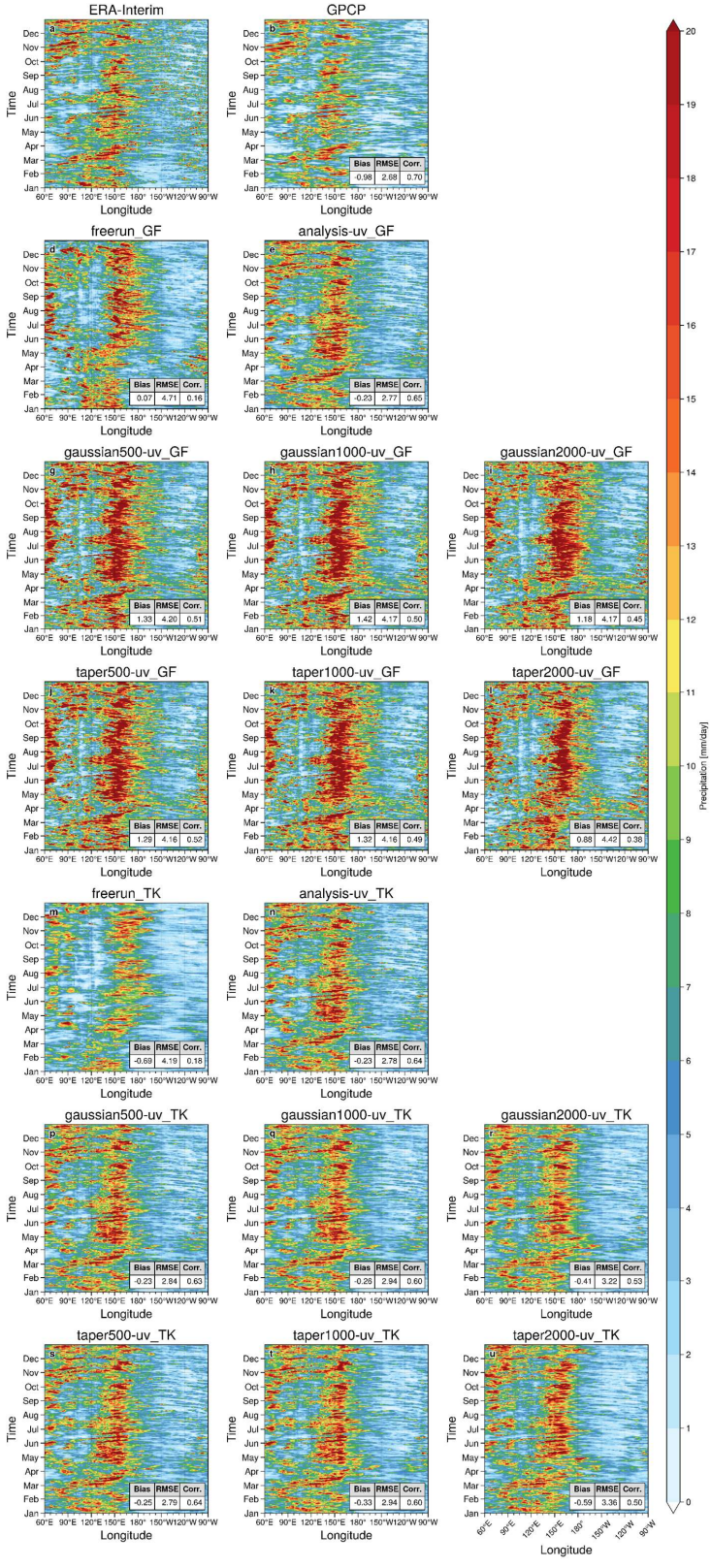

https://doi.org/10.5194/egusphere-2026-176
Preprint. Discussion started: 9 February 2026

Figure 3. Longitude–time distribution of daily precipitation averaged over 10°S–10°N, with the bottom-right inset showing summary pattern statistics for each case relative to ERA-Interim.

Figure 4 shows time–latitude cross section of daily precipitation averaged over the refined East Asian sector (60°–130°E, 10°–50°N), highlighting the seasonal migration of the mei-yu rainband. Freerun_TK rainfall is strongly concentrated in the deep tropics and along the southern edge of the monsoon domain. Freerun_GF captures the latitude of the subtropical rainband more realistically. The analysis-uv cases perform same in this regional cross-section for the two schemes. The panels indicate substantial pattern correlation (Corr ≈ 0.93) and a systematic underproduction of rainfall throughout the active monsoon phase (Bias≈-0.70 mm/day). For the spectral nudging cases, the large-scale structure and phase of the rainband are broadly preserved with similar pattern correlations under the same scheme. The dominant sensitivity instead lies in the rainfall amplitude. With the 500km constraint, the patterns converge toward the dry-bias state seen in the analysis cases, whereas the slighter constrained 2000km cases alleviates this dry bias and yields substantially lower RMSE.

https://doi.org/10.5194/egusphere-2026-176
Preprint. Discussion started: 9 February 2026

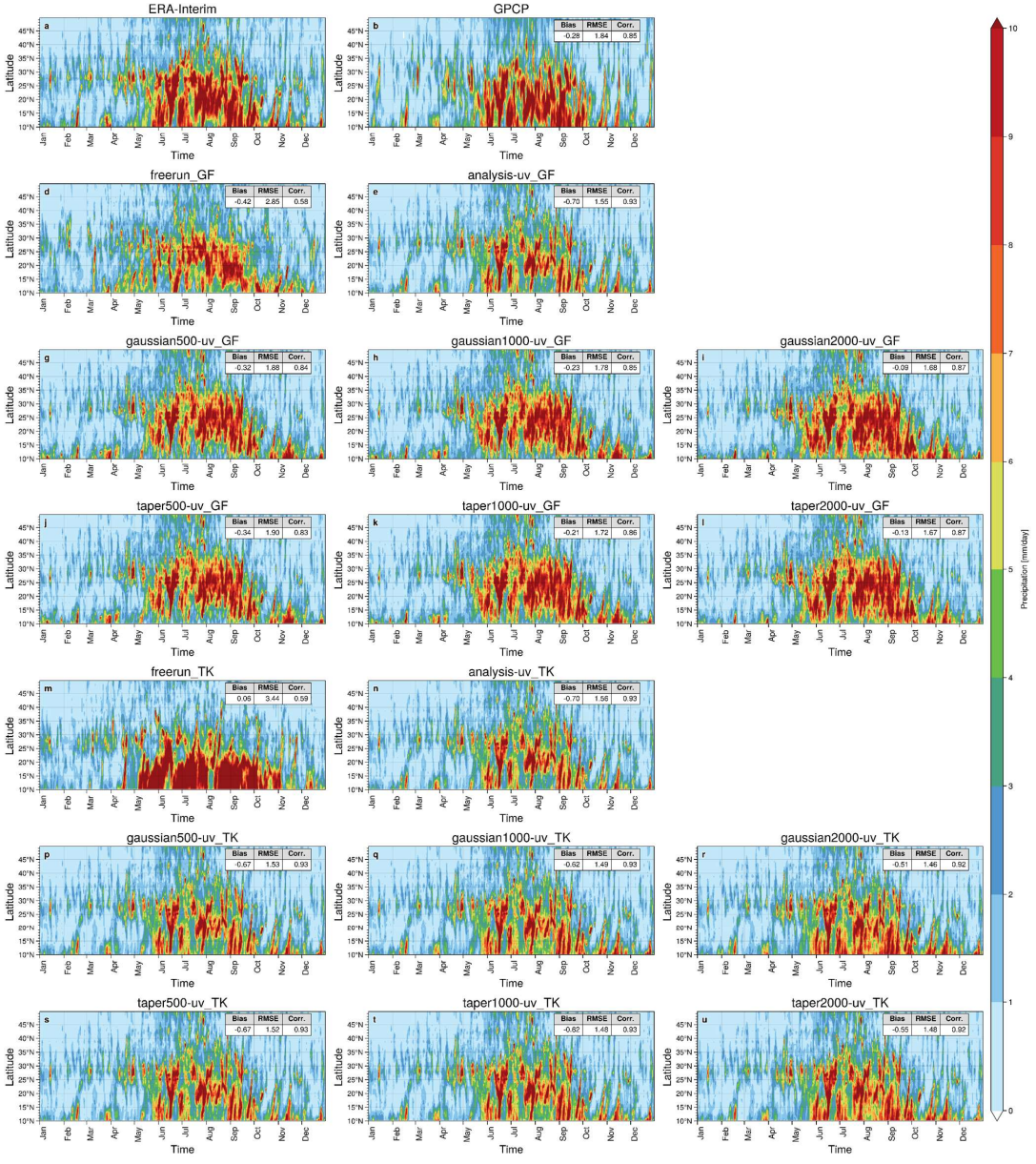

Figure 4. Latitude–time distribution of daily precipitation averaged over 60°E–130°E, with the top-left inset showing pattern statistics for each case relative to ERA-Interim.

Figure 5 shows the frequency distributions of daily precipitation amount, separated into the high-resolution and the coarser regions. The two convection suites exhibit markedly different cross-scale behavior. freerun_GF maintains almost identical frequency curves across resolutions. For freerun_TK, the coarse-resolution part closely follows the GPCP reference, whereas the high-resolution core more closely resembles the ERA-Interim–based distribution, implying a pronounced sensitivity of TK to grid spacing. An important consequence is that the strongest analysis constraint in GF degrades its otherwise good cross-scale performance. analysis-uv_GF develops a separation between resolutions that resembles the TK behavior, with the refined mesh no longer following the large-scale distribution. For the TK suites, relaxing the constraint from analysis

https://doi.org/10.5194/egusphere-2026-176
Preprint. Discussion started: 9 February 2026

nudging to slighter spectral nudging generally reduces the frequency at the heavy-rain tail. In the GF suites, the spectral nudging cases largely restore the scale adaptability of the precipitation frequency distribution. The high- and coarse-resolution curves become much more consistent with each other and converge back toward the behavior of freerun_GF.

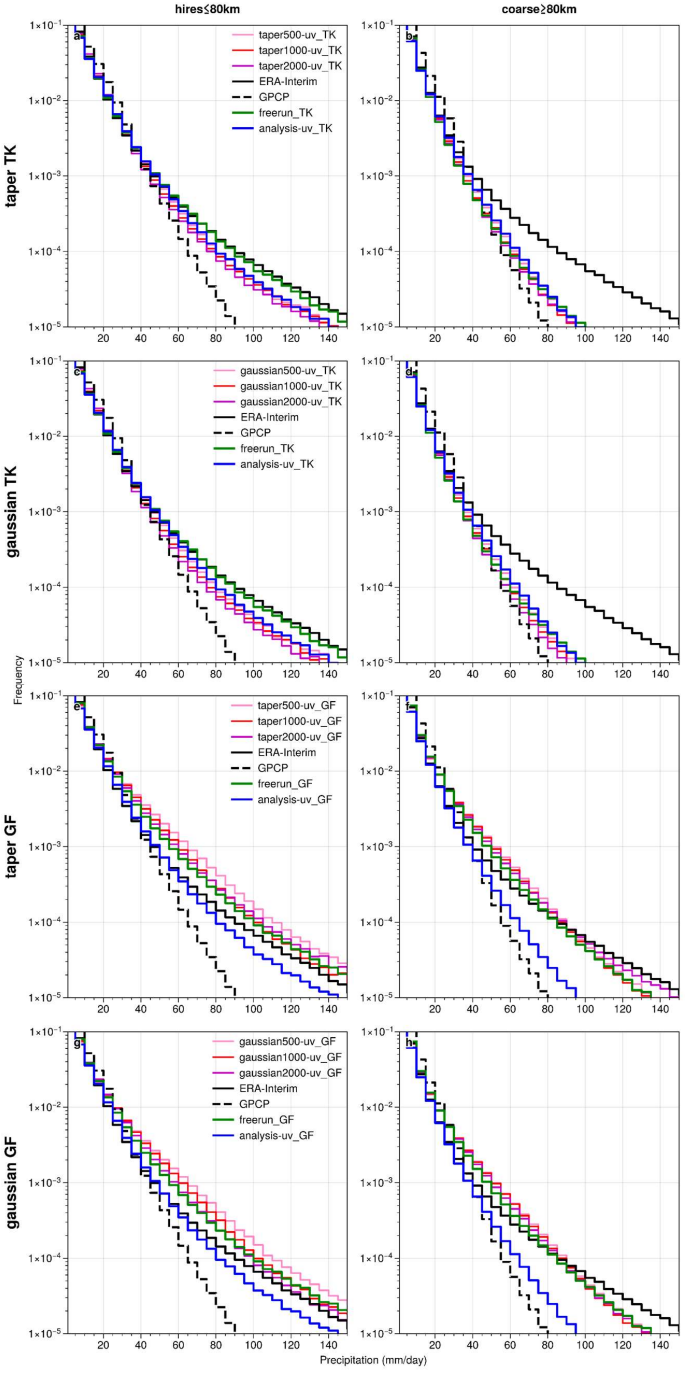

Figure 5. Frequency distributions of daily precipitation. The black solid line denotes ERA-Interim, the black dashed line denotes GPCP, the blue solid lines show the analysis nudging cases, and the green solid lines show the freerun cases. Purple, red, and pink solid lines indicate the spectral nudging cases with 2000 km, 1000 km, and 500 km filters, respectively. The first column shows the statistics over the refined region with grid spacing ≤80 km, and the second column corresponds to the coarse region with grid spacing >80 km. The top two rows present the TK suite, and the bottom two rows present the GF suite.

https://doi.org/10.5194/egusphere-2026-176
Preprint. Discussion started: 9 February 2026

4.3 Nudging Efficiency Across Spatial Scales

In the following, we use spatial kinetic energy spectra and temporal power spectra to diagnose how efficiently the nudging schemes act across a wide range of scales, and to clarify their cross-scale impacts on model variability. Figure 6 shows the kinetic energy spectra of 500-hPa wind speed with coefficients averaged at 6-hourly interval, together with their normalization by the corresponding freerun cases. All cases reproduce a robust -3 slope for wavelengths shorter than 1000 km, and ERA-Interim maintains this slope with the largest kinetic energy down to the smallest resolved scales. The freerun cases already show some loss of energy at high wavenumbers and this high-wavenumber damping is substantially amplified by nudging cases. Around 200 km the kinetic energy amplitudes of the analysis nudging cases are reduced to roughly one half of the freerun cases. The spectral nudging cases are designed to relax only large scales, and their normalized spectra clearly converges towards the analysis nudging curves at wavelengths longer than the prescribed nudging scale. However, the damp does not remain strictly confined to that scale. The impact is transmitted to smaller scales compared with the specified scale in the filter, and the energy reduction extends to higher wavenumbers. This cross-scale influence is especially evident in the two taper1000-uv cases, where the spectra start to deviate from the analysis nudging solution around 400 km, and then levels off with only weak additional damping towards smaller scales. Compared to the Gaussian filters, the Taper filters produce a sharper transition in the normalized spectra close to the target wavelength.

https://doi.org/10.5194/egusphere-2026-176
Preprint. Discussion started: 9 February 2026

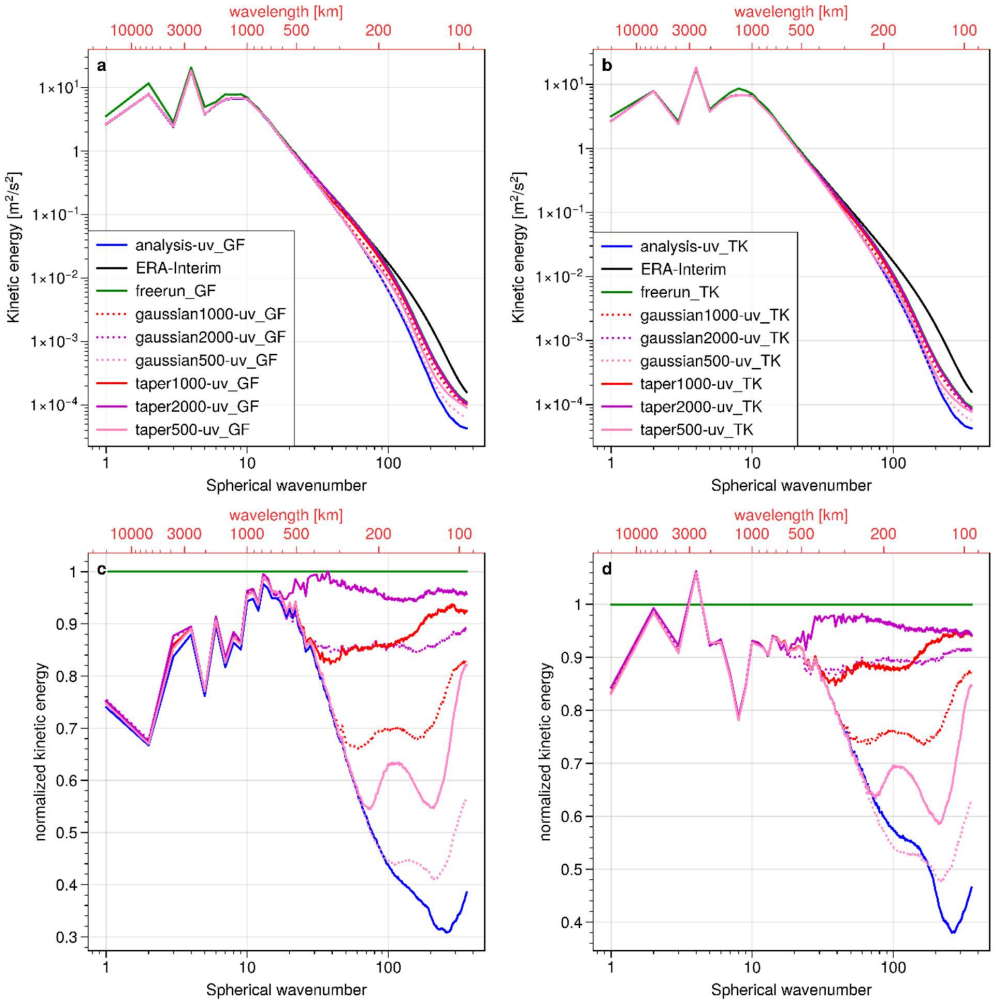

Figure 6. Kinetic energy spectra of 500-hPa wind. Panels (a–b) show the kinetic energy spectra computed from 6-hourly global winds over one year, with spectral coefficients averaged in time. Panels (c–d) show the same spectra normalized by the corresponding freerun case for each physics suite. Blue solid lines denote the analysis nudging cases, green solid lines the freerun cases, and purple, red, and pink lines the spectral nudging cases with 2000 km, 1000 km, and 500 km filters, respectively. Solid lines indicate Taper-filter cases, and dashed lines indicate Gaussian-filter cases.

Figure 7 further examines the cross-scale behaviors of the nudging schemes by combining the amplitude spectra of transient kinetic energy with the spectral coherence between the model and ERA-Interim at 500 hPa. The coherence, defined on the interval $[-1,1]$, measures the spatial phase consistency of transient eddies between the simulations and the reanalysis as a function of horizontal scale. At the largest scales, all nudging cases achieve coherence values close to one, indicating that the transient eddy patterns are tightly locked to the driving field. The analysis nudging cases show the strongest constraint. Their coherence remains high down to wavelengths of order 300 km, below which it rapidly decays. As the spectral nudging is relaxed to larger cutoff wavelengths, the scale at which coherence begins to drop systematically shifts to larger scales. In the amplitude spectra in Fig.7c–d, all cases show reduced amplitudes relative to ERA-Interim at small scales, the spectral nudging cases still preserve a substantial fraction of the freerun variance beyond the effective nudging scales. In particular, the taper2000-uv cases remain very close to the freerun cases in amplitude, and for wavelengths shorter than about 500 km they exhibit a similar roll-up of amplitude that reflects the model's internally generated eddies. The GF configuration even

https://doi.org/10.5194/egusphere-2026-176
Preprint. Discussion started: 9 February 2026

retains a freerun-like secondary maximum around 200–400 km in the Taper1000- and Taper2000-uv cases, whereas the TK configuration shows a smoother monotonic decay, pointing to subtle physics-dependent differences in how transient eddies respond to the same spectral nudging design.

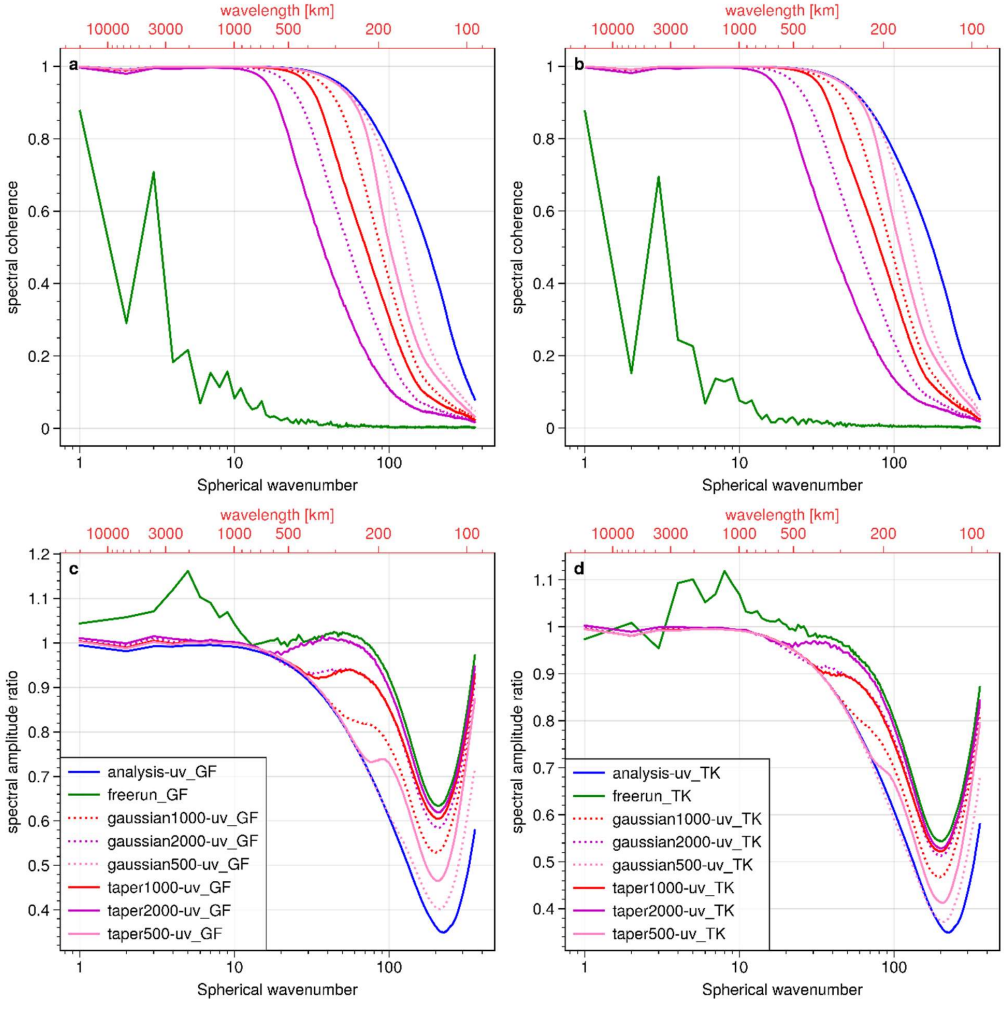

Figure 7. Scale-dependent spectral coherence and relative amplitude of transient 500-hPa wind kinetic energy. Panels (a–b) show the spatial spectral coherence between the model and ERA-Interim, computed from the time-mean cross- and auto-spectra of transient wind kinetic energy (deviations from the time mean). Panels (c–d) show the relative transient kinetic energy amplitude of the model with respect to the ERA-Interim reference at each spatial scale. Line colors and styles are identical to those in Figure 6.

Figure 8 presents the globally averaged temporal FFT amplitudes of 500-hPa zonal wind, normalized by the corresponding freerun cases. The spectra clearly reveal the imprint of the 6-hourly analysis update. All nudging cases exhibit a pronounced minimum at the 6-h period, indicating that variability at the nudging frequency is most strongly damped. This damping is largest in the analysis nudging cases, which provide an upper bound on the strength of the temporal constraint. Beyond this primary minimum, the spectra demonstrate the intended scale selectivity of the spectral nudging. high-frequency variability with periods shorter than about 48 h is increasingly retained as the nudging scale is relaxed, and the taper2000km-uv cases produce the smoothest and weakest damping (normalized amplitude above 0.9) across the spectrum.

https://doi.org/10.5194/egusphere-2026-176
Preprint. Discussion started: 9 February 2026

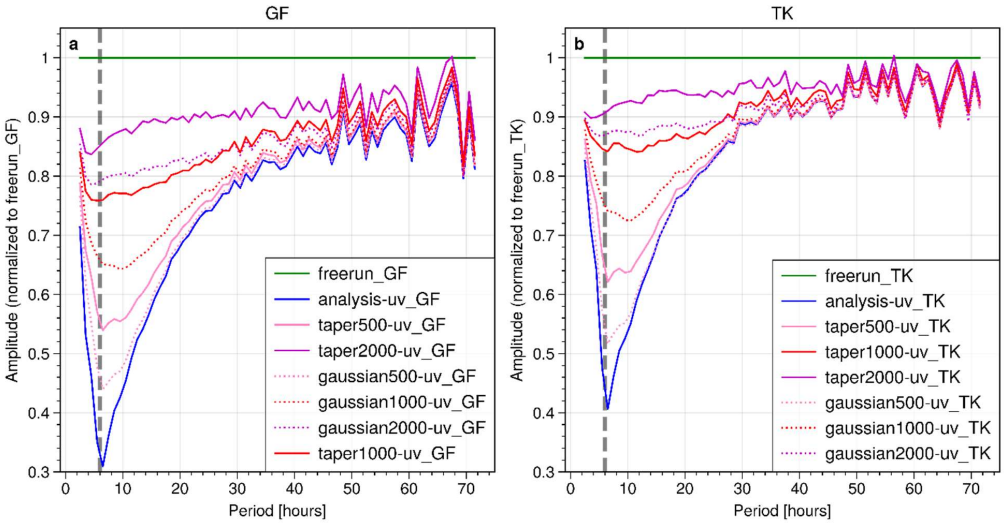

Figure 8. FFT amplitude spectra of globally averaged 1-hour zonal wind, normalized by the corresponding freerun case.

5 Conclusions

In this study we implemented a diffusion-based spectral nudging scheme in MPAS-A on an unstructured variable-resolution mesh and evaluated its behavior under two different convection schemes (GF and TK) and a range of filter scales and nudged variables. The main conclusions are as follows.

The analysis nudging on wind represents an upper bound on circulation control, but at the expense of both physics-scheme variability. The analysis nudging configurations exert the strongest constraint on the large-scale background, bringing upper-tropospheric jets and spatial patterns in GF and TK to an almost indistinguishable state. Consistently, the summary heatmaps of performance metrics indicate that analysis-uv_GF and analysis-uv_TK cluster tightly together across a wide range of diagnostics. In particular, the cross-scale adaptive behavior of the GF scheme—such as its consistent precipitation frequency distributions across resolutions and its more realistic positioning and intensity of East Asian rainfall in the freerun is largely lost when subjected to full analysis nudging.

In both GF and TK, diffusion-based spectral nudging interacts strongly with the physics scheme, so its strength, filter scale, and nudged variables must be tuned in a scheme-dependent way. TK exhibits a more robust and monotonic response to stronger spectral nudging and smaller filter scales, but it tends to converge toward the deficiencies of its analysis nudging baseline. This convergence also inherits shortcomings of analysis-uv_TK, including an overly deep and strong upper-tropospheric jet and a dry bias during the active East Asian monsoon season. In contrast, the GF suite shows a more discriminating response. Adding temperature nudging severely degrades performance, whereas adding moisture nudging yields the most consistent improvements across precipitation, OLR, precipitable water, and MSLP.

Spectral nudging partially rebuilds desirable freerun behavior. Spectral nudging using diffusion-based filters at 2000 km provides a compromise between the freerun and fully constrained analysis states. In the GF suites, these taper cases recover much of the favorable cross-scale behavior seen in the freerun cases. The precipitation frequency distributions become more consistent between the refined and coarse meshes, and the East Asian rainband regains more realistic intensity and latitude. For suitably chosen filter scales, especially the 500 km taper cases, both GF and TK produce top-of-atmosphere OLR and precipitable water that compare more favorably with the reanalysis than the corresponding analysis nudging baselines. Thus, taper filters allow the model to retain scale-adaptive aspects of the GF scheme and some beneficial freerun characteristics,

https://doi.org/10.5194/egusphere-2026-176
Preprint. Discussion started: 9 February 2026

while selectively improving large-scale circulation and hydrological mean-state metrics beyond what is achieved by the strongly constrained analysis cases.

The spectral diagnostics demonstrate that diffusion-based spectral nudging is effective at locking the large-scale circulation and transient eddies to the reanalysis while maintaining a substantial fraction of the freerun variance at smaller scales. Kinetic energy spectra show that, beyond the nominal nudging wavelength, taper and Gaussian filters reduce energy toward the analysis nudging level, but taper filters create a sharper transition and allow the small-scale tail to remain closer to the freerun. Coherence spectra indicate that transient eddies are nearly perfectly phase-locked to the reference at synoptic scales in all nudging runs, with the scale at which coherence decays shifting systematically with the chosen cutoff. Temporal FFT analysis further reveals that the nudging imprint is strongest at the 6-hour update period, whereas high-frequency variability (periods < ~2 days) is increasingly retained as the nudging scale is relaxed, with the 2000-km taper cases preserving more than ~90% of the freerun amplitude across most of the spectrum.

Overall, our findings suggest that diffusion-based spectral nudging on unstructured meshes is a powerful tool for "specified-dynamics" style MPAS-A simulations, but its benefits depend critically on a three-way balance between filter design, nudging variables, and the underlying physics suite. Carefully tuned spectral nudging can enhance cross-scale consistency and reduce large-scale biases without unduly sacrificing transient variability. In this sense, diffusion-based spectral nudging provides an effective trade-off: it keeps the large-scale flow and transient eddies closely phase-locked to the analysis while still allowing the model sufficient freedom at smaller scales to express scheme-dependent behavior. Rather than completely suppressing variability as in full analysis nudging, it preserves the multiscale signals needed to diagnose how different physics schemes shape the solution.

Code and data availability

The MPAS-A spectral nudging implementation used in this study is openly available at: https://doi.org/10.5281/zenodo.18229522. This repository contains a modified version of MPAS-A (v8.2.2) that ports the analysis nudging scheme of Bullock Jr. et al. (2018) to MPAS-A v8.2.2, including non-selective nudging and resolution-scaled nudging tendencies, and introduces a diffusion-based spatial filtering module to enable scale-selective nudging. The ERA-Interim reanalysis data used for the initial and boundary conditions in the MPAS-A experiments were obtained from ECMWF (Dee et al., 2011).

Author contributions

YYC designed and performed the experiments, developed and implemented the model code, carried out the simulations, and conducted the data analysis and visualization. JPT provided computational resources and technical support, reviewed the model code, and contributed to the interpretation of results. YYC and JPT wrote the manuscript, and JPT reviewed and edited the manuscript. Both authors discussed the results and approved the final version.

Competing interests

The contact author has declared that none of the authors has any competing interests.

https://doi.org/10.5194/egusphere-2026-176
Preprint. Discussion started: 9 February 2026

Acknowledgements

The numerical calculations in this paper have been done on the computing facilities in the High Performance Computing Center (HPCC) of Nanjing University. The authors acknowledge with thanks the ECMWF for providing the ERA-interim reanalysis data.

Financial support

This study was funded by the National Key Research and Development Program of China (grant no. 2023YFF0805404) and the S&T Development Fund of CAMS (2025KJ022).

References

Alexandru, A., Elía, R., Laprise, R., Separovic, L., and Biner, S.: Sensitivity study of regional climate model simulations to large-scale nudging parameters, Monthly Weather Review, 137, 1666–1686, https://doi.org/10.1175/2008MWR2620.1, 2009.

Anthes, R. A.: Data assimilation and initialization of hurricane prediction models, Journal of the Atmospheric Sciences, 31, 702–719, https://doi.org/10.1175/1520-0469(1974)031<0702:DAAIOH>2.0.CO;2, 1974.

Bullock Jr., O. R., Foroutan, H., Gilliam, R. C., and Herwehe, J. A.: Adding four-dimensional data assimilation by analysis nudging to the Model for Prediction Across Scales – Atmosphere (version 4.0), Geoscientific Model Development, 11, 2897–2922, https://doi.org/10.5194/gmd-11-2897-2018, 2018.

Chen, F., and Dudhia, J.: Coupling an Advanced Land Surface–Hydrology Model with the Penn State–NCAR MM5 Modeling System, Part I: Model Implementation and Sensitivity. Monthly Weather Review, 129, 569–585, https://doi.org/10.1175/1520-0493(2001)129<0569:CAALSH>2.0.CO;2, 2001.

Davis, N. A., Callaghan, P., Simpson, I. R., and Tilmes, S.: Specified dynamics scheme impacts on wave-mean flow dynamics, convection, and tracer transport in CESM2 (WACCM6), Atmospheric Chemistry and Physics, 22, 197–214, https://doi.org/10.5194/acp-22-197-2022, 2022.

Dee, D. P., Uppala, S. M., Simmons, A. J., Berrisford, P., Poli, P., Kobayashi, S., et al.: The ERA-Interim reanalysis: configuration and performance of the data assimilation system, Quarterly Journal of the Royal Meteorological Society, 137, 553–597, https://doi.org/10.1002/qj.828, 2011.

Germano, M.: Differential filters for the large eddy numerical simulation of turbulent flows, The Physics of Fluids, 29, 1755–1757, https://doi.org/10.1063/1.865649, 1986.

Grooms, I., Loose, N., Abernathey, R., Steinberg, J. M., Bachman, S. D., Marques, G., Guillaumin, A. P., and Yankovsky, E.: Diffusion-based smoothers for spatial filtering of gridded geophysical data, Journal of Advances in Modeling Earth Systems, 13, e2021MS002552, https://doi.org/10.1029/2021MS002552, 2021.

Grell, G. A., and Freitas, S. R.: A scale and aerosol aware stochastic convective parameterization for weather and air quality modeling, Atmospheric Chemistry and Physics, 14, 5233–5250, https://doi.org/10.5194/acp-14-5233-2014, 2014.

https://doi.org/10.5194/egusphere-2026-176
Preprint. Discussion started: 9 February 2026

Guedot, L., Lartigue, G., and Moureau, V.: Design of implicit high-order filters on unstructured grids for the identification of large-scale features in large-eddy simulation and application to a swirl burner, Physics of Fluids, 27, 045107, https://doi.org/10.1063/1.4917280, 2015.

He, X., Tang, J., Ma, M., Lu, Y., and Xu, Y.: Convection-permitting regional reanalysis experiment over China: Evaluation of summer precipitation in 2020, Atmospheric Research, 328, 108412, https://doi.org/10.1016/j.atmosres.2025.108412, 2025.

Hong, S. Y. and Lim, J. O. J.: The WRF single-moment 6-class microphysics scheme (WSM6), Asia-Pacific Journal of Atmospheric Sciences, 42, 129–151, 2006.

Hong, S. Y.: A new stable boundary-layer mixing scheme and its impact on the simulated East Asian summer monsoon, Quarterly Journal of the Royal Meteorological Society, 136, 1481–1496, https://doi.org/10.1002/qj.665, 2010.

Huffman, G. J., Bolvin, D. T., Braithwaite, D., Hsu, K., Joyce, R., and Xie, P.: NASA Global Precipitation Measurement (GPM) Integrated Multi-satellite Retrievals for GPM (IMERG), NASA GPM [data set], https://gpm.nasa.gov/data/imerg (last access: 13 January 2026), 2014.

Iacono, M. J., Mlawer, E. J., Clough, S. A., and Morcrette, J.-J.: Impact of an improved longwave radiation model, RRTM, on the energy budget and thermodynamic properties of the NCAR community climate model, CCM3, Journal of Geophysical Research: Atmospheres, 105, 14873–14890, https://doi.org/10.1029/2000JD900091, 2000.

Kao, C.-Y. J. and Yamada, T.: Use of the CAPTEX data for evaluations of a long-range transport numerical model with a four-dimensional data assimilation technique, Monthly Weather Review, 116, 293–306, https://doi.org/10.1175/1520-0493(1988)116<0293:UOTCDF>2.0.CO;2, 1988.

Kooperman, G. J., Pritchard, M. S., Ghan, S. J., Wang, M., Somerville, R. C. J., and Russell, L. M.: Constraining the influence of natural variability to improve estimates of global aerosol indirect effects in a nudged version of the Community Atmosphere Model 5, Journal of Geophysical Research: Atmospheres, 117, D23204, https://doi.org/10.1029/2012JD018588, 2012.

Lin, G., Wan, H., Zhang, K., Qian, Y., and Ghan, S. J.: Can nudging be used to quantify model sensitivities in precipitation and cloud forcing, Journal of Advances in Modeling Earth Systems, 8, 1073–1091, https://doi.org/10.1002/2016MS000659, 2016.

Loose, N., Abernathey, R., Grooms, I., Bachman, S., Marques, G., and Feng, J.: GCM-Filters: A Python Package for Diffusion-based Spatial Filtering of Gridded Data (Version v0.2.1) [code], GitHub, https://github.com/ocean-eddy-cpt/gcm-filters (last access: 13 January 2026), 2022.

Miguez-Macho, G., Stenchikov, G. L., and Robock, A.: Spectral nudging to eliminate the effects of domain position and geometry in regional climate model simulations, Journal of Geophysical Research: Atmospheres, 109, D13104, https://doi.org/10.1029/2003JD004495, 2004.

Mlawer, E. J., Taubman, S. J., Brown, P. D., Iacono, M. J., and Clough, S. A.: Radiative transfer for inhomogeneous atmospheres: RRTM, a validated correlated-k model for the longwave, Journal of Geophysical Research: Atmospheres, 102, 16663–16682, https://doi.org/10.1029/97JD00237, 1997.

Schaaf, B., von Storch, H., and Feser, F.: Does spectral nudging have an effect on dynamical downscaling?, Monthly Weather Review, 145, 4303–4311, https://doi.org/10.1175/MWR-D-17-0087.1, 2017.

Separovic, L., de Elía, R., and Laprise, R.: Impact of spectral nudging and domain size in studies of RCM response to parameter modification, Climate Dynamics, 38, 1325–1343, https://doi.org/10.1007/s00382-011-1072-7, 2012.

Skamarock, W. C., Klemp, J. B., Duda, M. G., Fowler, L. D., Park, S.-H., and Ringler, T. D.: A Multiscale Nonhydrostatic Atmospheric Model Using Centroidal Voronoi Tesselations and C-Grid Staggering, Monthly Weather Review, 140, 3090–3105, https://doi.org/10.1175/MWR-D-11-00215.1, 2012.

https://doi.org/10.5194/egusphere-2026-176
Preprint. Discussion started: 9 February 2026

Stauffer, D. R. and Seaman, N. L.: Use of four-dimensional data assimilation in a limited-area mesoscale model. Part I: Experiments with synoptic-scale data, Monthly Weather Review, 118, 1250–1277, https://doi.org/10.1175/1520-0493(1990)118<1250:UOFDDI>2.0.CO;2, 1990.

Storch, H., Langenberg, H., and Feser, F.: A Spectral Nudging Technique for Dynamical Downscaling Purposes, Monthly Weather Review, 128, 3664–3673, https://doi.org/10.1175/1520-0493(2000)128<3664:ASNTFD>2.0.CO;2, 2000.

Sun, J., Zhang, K., Wan, H., Ma, P.-L., Tang, Q., and Zhang, S.: Impact of Nudging Strategy on the Climate Representativeness and Hindcast Skill of Constrained EAMv1 Simulations, Journal of Advances in Modeling Earth Systems, 11, 3911–3933, https://doi.org/10.1029/2019MS001831, 2019.

Tang, J., Wang, S., Niu, X., Hui, P., Zong, P., and Wang, X.: Impact of spectral nudging on regional climate simulation over CORDEX East Asia using WRF, Climate Dynamics, 48, 2339–2357, https://doi.org/10.1007/s00382-016-3208-2, 2017.

Thatcher, M. and McGregor, J.: Using a scale-selective filter for dynamical downscaling with the conformal cubic atmospheric model, Monthly Weather Review, 137, 1742–1752, https://doi.org/10.1175/2008MWR2599.1, 2009.

Thompson, G., Field, P. R., Rasmussen, R. M., and Hall, W. D.: Explicit Forecasts of Winter Precipitation Using an Improved Bulk Microphysics Scheme, Part II: Implementation of a New Snow Parameterization. Monthly Weather Review, 136, 5095–5115, https://doi.org/10.1175/2008MWR2387.1, 2008.

Tweedy, O. V., Limpasuvan, V., Orsolini, Y. J., Smith, A. K., Garcia, R. R., Kinnison, D., et al.: Nighttime secondary ozone layer during major stratospheric sudden warmings in specified-dynamics WACCM, Journal of Geophysical Research: Atmospheres, 118, 8346–8358, https://doi.org/10.1002/jgrd.50651, 2013.

Uhe, P., and Thatcher, M.: A spectral nudging method for the ACCESS1.3 atmospheric model, Geoscientific Model Development, 8, 1645–1658, https://doi.org/10.5194/gmd-8-1645-2015, 2015.

Waldron, K. M., Paegle, J., and Horel, J. D.: Sensitivity of a spectrally filtered and nudged limited-area model to outer model options, Monthly Weather Review, 124, 529–547, https://doi.org/10.1175/1520-0493(1996)124<0529:SOASFA>2.0.CO;2, 1996.

Yoshimura, K. and Kanamitsu, M.: Dynamical global downscaling of global reanalysis, Monthly Weather Review, 136, 2983–2998, https://doi.org/10.1175/2008MWR2281.1, 2008.

Zhang, C., Wang, Y., and Hamilton, K.: Improved Representation of Boundary Layer Clouds over the Southeast Pacific in ARW-WRF Using a Modified Tiedtke Cumulus Parameterization Scheme, Monthly Weather Review, 139, 3489–3513, https://doi.org/10.1175/MWR-D-10-05091.1, 2011.

Zhang, K., Wan, H., Liu, X., Ghan, S. J., Kooperman, G. J., Ma, P.-L., Rasch, P. J., Neubauer, D., and Lohmann, U.: Process-oriented constraints on global aerosol indirect effects from a multiple model evaluation, Atmospheric Chemistry and Physics, 14, 8631–8655, https://doi.org/10.5194/acp-14-8631-2014, 2014.